

ARTICLES

Compton scattering from the proton

E. L. Hallin, D. Amendt, J. C. Bergstrom, H. S. Caplan, R. Igarashi, and D. M. Skopik
Saskatchewan Accelerator Laboratory, University of Saskatchewan, Saskatoon, Saskatchewan, Canada S7N 0W0

E. C. Booth, D. Delli Carpini, and J. P. Miller
Department of Physics, Boston University, 590 Commonwealth Avenue, Boston, Massachusetts 02215

F. J. Federspiel, B. E. MacGibbon, and A. M. Nathan
Department of Physics, University of Illinois at Urbana-Champaign, Nuclear Physics Laboratory, Champaign, Illinois 61820

(Received 12 April 1993)

The proton Compton effect has been studied in the region between the threshold for pion photoproduction and the $\Delta(1232)$. The measurements were performed using bremsstrahlung from the high duty-factor electron beam available at the Saskatchewan Accelerator Laboratory. Elastically scattered photons were detected with an energy resolution of approximately 1.5% using a large NaI total absorption scintillation detector. Differential cross sections were measured for photon energies in the range $136 \text{ MeV} \leq E_\gamma \leq 289 \text{ MeV}$ and for angles in the range $25^\circ < \theta_{\text{lab}} < 135^\circ$. The angular distributions and the excitation functions derived from these data are in agreement with recent theoretical analyses. The results were interpreted within a formalism based in part on dispersion relations to obtain model-dependent estimates of the electric and magnetic polarizabilities, $\bar{\alpha}$ and $\bar{\beta}$. We find, subject to the dispersion sum rule constraint $\bar{\alpha} + \bar{\beta} = (14.2 \pm 0.5) \times 10^{-4} \text{ fm}^3$, that $\bar{\alpha} = (9.8 \pm 0.4 \pm 1.1) \times 10^{-4} \text{ fm}^3$ and $\bar{\beta} = (4.4 \mp 0.4 \mp 1.1) \times 10^{-4} \text{ fm}^3$, which are consistent with the best previous measurements.

PACS number(s): 25.20.Dc

I. INTRODUCTION

Compton scattering from the proton is of interest since, in this interaction, the most elementary nuclear system is examined by the most elementary probe. At energies far below the threshold for pion photoproduction, the cross section for Compton scattering from the proton is described by photon coupling to a structureless spin- $\frac{1}{2}$ particle of the appropriate charge, mass, and anomalous magnetic moment [1]. In this energy regime, Compton scattering is mostly sensitive to the first term of the electromagnetic Hamiltonian

$$H = j_\mu A^\mu - \frac{1}{2} S_{\mu\nu} A^\mu A^\nu. \quad (1)$$

At photon energies comparable to the threshold for pion photoproduction, the incident photon begins to couple to the mesonic cloud associated with the proton and the effects of these mesonic degrees of freedom are buried in the quadratic (seagull) term in the Hamiltonian. The seagull term is related to the electromagnetic current through gauge invariance, but it is directly accessible only through two photon processes such as Compton scattering, and depends on the explicit mesonic degrees of freedom included in the Hamiltonian [2,3]. Nuclear Compton scattering directly probes this term allowing the electric and magnetic polarizabilities of the proton to be measured, and at sufficiently low energies a comparison with theory can be done in a relatively model-

independent way [4]. Once pion threshold has been reached, however, the (γ, π) and (π, N) interactions must be taken into account in order to predict the nuclear Compton scattering cross section. Using dispersion theory together with the analyticity of the photon scattering amplitudes, the real parts of the scattering amplitudes can be calculated if the imaginary parts are known. Fortunately, the latter are well known from photoabsorption studies. This dispersion theory approach has been developed by several groups [5–8] with the most recent and extensive work being due to L'vov [3]. In the latter formalism, Compton scattering from the proton can be described with only two free parameters, namely, the electric and magnetic polarizabilities of the proton. Furthermore, the sum of these polarizabilities is constrained in a model-independent way by the dispersion sum rule [9]

$$\bar{\alpha} + \bar{\beta} = (14.2 \pm 0.5) \times 10^{-4} \text{ fm}^3, \quad (2)$$

so there remains only the difference $\bar{\alpha} - \bar{\beta}$ as the free parameter in the theory. Thus, above the pion photoproduction threshold, Compton scattering by the proton can yield the polarizabilities subject to a knowledge of the (γ, π) and (π, N) processes. Finally, as the Δ resonance is approached, the interaction with this additional degree of freedom can also be explored. In fact, it was a desire to examine Δ -hole models of Compton scattering from nuclei which motivated the experimental program (Comp-

ton scattering from ^1H , ^4He , and ^{12}C) of which the present measurement is one part [10].

Elastic photon scattering from the proton has been investigated by a number of groups in the region of the $\Delta(1232)$ resonance [11–15]. Near the Δ , the experiments are difficult due to the combination of the low Compton scattering cross section and the high cross section for the dominant background process, which is the decay of photoproduced neutral pions. The technique usually adopted in the early experiments was to suppress the background by detecting both the recoil proton and the photon in coincidence. Unfortunately, poor energy resolution and difficulties in measuring the photon flux complicated the interpretation of these data. In addition, the experimental techniques restricted the minimum scattering angles, so complete angular distributions were not measured in these early experiments. Only recently have improvements in accelerator and detector technology allowed a fresh look at this field.

Our experiment provides the first high-resolution, systematic study of the proton Compton effect in the energy regime between 136 and 289 MeV. The quality and extent of the resulting angular distributions have fulfilled our original goal of extending the world's database in this region, and have allowed us to extract estimates of the electric and magnetic polarizabilities of the proton. Since our data span the threshold for pion photoproduction, we have also been able to examine the energy dependence of the differential cross sections near threshold.

II. EXPERIMENTAL METHOD

Compton scattering cross sections on the proton were measured at the Saskatchewan Accelerator Laboratory (SAL). A diagram of experimental area 2 (EA2) at SAL is shown in Figs. 1(a) and 1(b). (This experimental area has recently been greatly expanded.) An electron beam with a duty factor of about 50% was used to produce a bremsstrahlung photon beam by intercepting a 0.01 radiation length aluminum radiator. The bremsstrahlung end-point energies were 170, 200, 244, and 298 MeV. The primary electron beam current was monitored by measuring the charge deposited in a water-cooled beam stop. A 1-cm-diam by 30-cm-long lead collimator together with 1 m of dense concrete shielding plus a sweep magnet were used to obtain a clean 2.5-cm-diam photon beam. The liquid-hydrogen target was a 10.2-cm-diam by 12.7-cm-long cylinder made of 35-mg/cm² Mylar, and was wrapped with 10 layers of aluminized Mylar "super-insulation." The target was in thermal contact with a recondensing refrigerator that maintained the temperature of the liquid at approximately 20 K. A thin copper radiation shield at 77 K surrounded the vessel. The photon detector was the high-resolution total absorption NaI(Tl) scintillation counter designed at Boston University [16]. It consists of a cylindrical core of NaI surrounded by four annular NaI quadrants. NaI is encased in a plastic scintillator annulus which, together with plastic veto counters in front of and behind the detector, was used to reject the cosmic ray background with 98.5% efficiency. Cosmic rays can be identified off line by com-

paring relative energy deposition in the core with that in the quadrants, and the result of this additional cut is an overall rejection efficiency of 99.995%. Neutron backgrounds were reduced to acceptable levels through careful geometrical shielding of the detector. A 12.7-cm-diam, 7.6-cm-thick tungsten collimator defined the detector aperture. The photon flux was continuously monitored by measuring the energy deposited in a Wilson-type quantameter which was well shielded from room backgrounds. The charge measured by this quantameter is proportional to the total energy deposited in the quantameter. The calibration constant was measured both at Bates and at SAL and the two values are consistent within error; the value used in the present work is $(1.02 \pm 0.03) \times 10^{19}$ MeV per Coulomb [17].

Figures 1(a) and 1(b) together illustrate how one particular experimental problem was solved. The target together with its ancillary apparatus (not shown in the figures) and the detector with its shielding occupied a

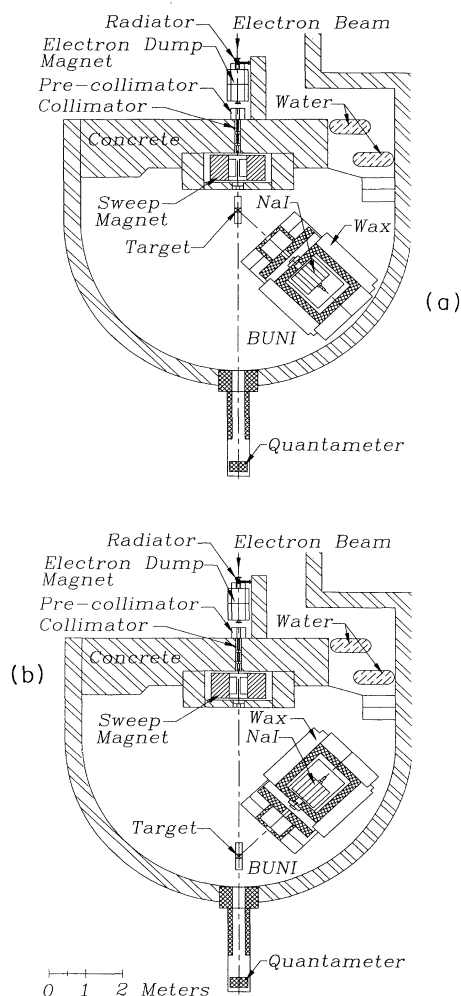


FIG. 1. A scale diagram of experimental area 2 (EA2) at SAL, showing the detector and its shielding at a forward-angle (a) and for a back-angle measurement (b).

significant fraction of the experimental hall. The detector was mounted on air pads which allowed it to be moved almost anywhere in the hall, while the target was suspended from a rail attached to the ceiling. This rail was parallel to the beam line and directly above it, so that the hydrogen target could be rolled back and forth along the beam line. For forward-angle measurements the target was shifted upstream and the detector was oriented towards the front of the hall. This configuration is shown in Fig. 1(a). For backward-angle measurements, the target was rolled as far downstream as possible and the detector was oriented to face the back of the hall, as shown in Fig. 1(b). Thus, the volume of the target illuminated by the photon beam varied from angle to angle, as did the solid angle subtended by the detector.

Each optically isolated part of the NaI crystal was viewed with several Hamamatsu R1911 photomultiplier tubes. Gains were monitored during the measurement with a xenon light flasher and fiber optic cables that delivered the “same” light flash to each NaI segment. A small well-shielded NaI crystal monitored a thorium source and allowed the output of the xenon flasher itself to be stabilized to $\pm 0.5\%$. Periodically a thorium source was placed in the aperture of the detector to allow the gains of the quadrants to be monitored. This procedure was less crucial than the gain monitoring of the central core since only a small fraction of the shower leaked into the NaI annulus. It was important, however, in obtaining the ultimate energy resolution of about 1.5% FWHM.

A 42-gm/cm² solid beryllium absorber was placed in front of the collimator to remove low-energy electrons and photons, reducing pileup. Veto scintillators rejected charged particles produced in this absorber. To further reduce pileup, the NaI signals were clipped to approximately 600-ns duration. With typical rates in the NaI of 40 kHz above a few MeV threshold, resulting in trigger rates of 50 Hz above a 100-MeV threshold, the pileup was reduced to the acceptable level of a few percent. A separate discriminator with a very low threshold level allowed on-line monitoring of the pileup rate which was used to adjust beam current. Electron beam currents were typically about 1 μ A, producing a photon flux of approximately 1.2×10^7 photons per MeV per s over the “interesting” portion of the bremsstrahlung spectrum near the end point.

A series of target-empty and target-full runs were performed at each scattering angle. A typical full-empty cycle required about 6–8 h and, depending on the energy and angle, each data run required roughly 1 day to acquire acceptable statistics in the photon yield region of interest. A pulse-height spectrum for an endpoint energy of 200 MeV and $\theta_{\text{lab}} = 135^\circ$ is shown in Fig. 2. The kinematic region of interest should contain only elastically scattered photons, and it is defined by the interval between the most energetic photon possible from the decay of photoproduced neutral pions and the kinematic end point. The approximate extent of this region is indicated in the figure by the thick horizontal line. The upper end of the large π^0 background is clearly visible at the left side of the figure.

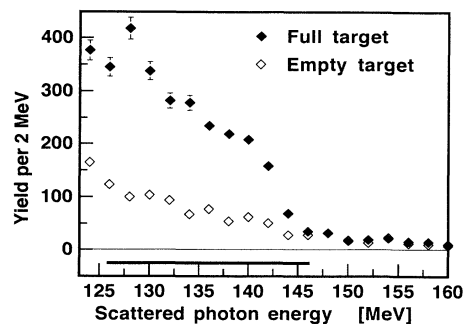


FIG. 2. Scattered photon yields for an incident electron energy of 200 MeV at a laboratory angle of 134.8° . The region of interest is delineated by the horizontal line. The left-most edge of this region is just above the π^0 decay end point and the right-most edge is at the kinematic end point.

III. DATA REDUCTION

A. Calibration of the detector

For each beam energy, the response of the detector was determined by rotating it to 0° where a greatly reduced photon flux directly entered the crystal. The absolute energy calibration of the detector response was then determined by fitting an EGS4 [18] simulated detector response function to the measured 0° spectrum. The simulated response function was calculated using an incident bremsstrahlung spectrum of the appropriate end-point energy [19], so that fitting the measured and calculated detector response curves established an energy calibration relative to the accelerator endpoint energy. The photomultiplier tube gains were monitored and corrected to an accuracy of 0.5% (as determined by comparing the expected gain and the subsequent absolute gain measurement) on a run-by-run basis. The energy-calibrated yield shown in Fig. 2 is representative of the data taken in this experiment.

B. Background subtraction

A target-empty yield spectrum is also shown in Fig. 2. The two main sources of background contributing in this figure are cosmic rays and photons which scatter from the target windows. Approximately 0.005% of the cosmic flux passed all the software cuts. Since the cosmic background is not correlated with the beam, it was corrected by subtracting time-normalized beam-off yields from the full- and empty-target yields. The backgrounds correlated with the photon beam accounted for nearly all of the empty-target spectra in the region of interest, and were removed by subtracting the empty-target spectra (normalized to the incident photon flux measured with the quantameter) from the full-target spectra. A further correction was made for the fact that about 2% of the hydrogen remained in the target cell during the “empty” target runs, after which the total flux in the region above the kinematic end point was consistent with zero for all energies and angles measured.

C. Simulation of the detector response

Figure 3 shows a background-corrected spectrum together with a simulation which takes into account both Compton scattering in the target and the decay of neutral pions. The photon spectrum from these two principal source is well modeled by the detector simulation described below. The primary photon in each case was sampled from a calculated bremsstrahlung distribution of the appropriate end-point energy.

The π^0 decay spectral shapes were determined using a technique first reported by Cocconi and Silverman [20] together with the photoproduction cross-section compilation of Genzel, Joos, and Pfeil [21]. Cocconi and Silverman parametrize the angular dependence of the π^0 photoproduction cross section as $A + B \cos^2\theta$ and then use this to develop an analytic expression for the energy and angular distribution of the decay photons. We have performed a least-squares fit to the tabulated photoproduction cross sections on the proton to determine A and B as a function of energy over the entire range of energies of interest for the present analysis. A Monte Carlo technique was used to fold this distribution with the incident bremsstrahlung spectrum. The resulting spectral shape was then used as the distribution from which to randomly sample photons to act as inputs for the EGS4 simulation of the detector. Using this technique, a simulated π^0 decay response curve was calculated for each energy and angle of the experiment.

A similar procedure was employed to simulate the detector response to a Compton scattered bremsstrahlung spectrum. In this case the sampling process was much simpler, although an iterative procedure had to be developed since the Compton scattering cross section must eventually be used as an input to this calculation. To begin this process, each photon was randomly sampled from an incident bremsstrahlung spectrum and then allowed (with unit probability) to Compton scatter. This process is explicitly energy independent, and so the resulting curves would only be valid to the extent that the Compton cross section is independent of energy. The calculated curves were then summed and the data analysis was carried through to completion, as discussed below.

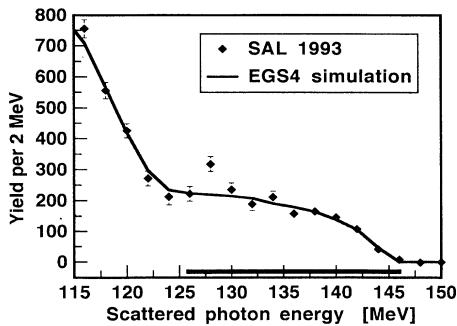


FIG. 3. A comparison between the normalized EGS4 simulation of the detector response and the background-subtracted yield spectrum. The simulated spectrum is normalized to the area of the measured spectrum in the region of interest.

Once the energy dependence of the Compton scattering cross sections had been determined, it was then used in the photon sampling procedure to generate a new set of theoretical curves and once again the analysis was carried through to completion. After four iterations, the extracted cross sections changed by much less than the statistical error with which they were measured and the procedure was stopped.

The two calculated response curves were then summed and normalized to the data in the region of interest. Note that this procedure is not a fit, but only a normalization. The success of this method is evident from the good agreement between the normalized simulated detector response curve and the background subtracted data shown in Fig. 3.

The simulation of the detector response was of crucial significance in the extraction of absolute cross sections since the determination of the detector efficiency is dependent on successfully predicting the shape of the detector response. For any given energy window in the detected spectrum, the detection efficiency was calculated by comparing the integral of the simulated response with the known total flux in the same window. Since the response simulation included the effects of absorption in the material between the target and the detector as well as the intrinsic efficiency of the detector, both of these effects are included in the calculation of the detection efficiency. A similar technique has been successfully applied in two independent analyses of helium and carbon Compton scattering data acquired with the same apparatus.^{22,23}

The sharp edge of the π^0 decay spectrum also served as a check on the energy calibration of the detector. The small “excursion” visible at about 129 MeV is not due to π^- capture in hydrogen since it is not evident in the other energy and angle combinations.

Once we are satisfied that our simulation is an accurate representation of the data, we then use that simulation to obtain the efficiency $\varepsilon(E_1, E_2)$ for detecting a scattered photon in the pulse-height window between E_1 and E_2 .

D. Cross-section extraction

The differential cross sections were calculated according to the expression

$$\begin{aligned} \frac{d\sigma_{\text{c.m.}}}{d\Omega}(\theta_{\text{c.m.}}, \bar{E}) &= \frac{d\sigma}{d\Omega}(\theta, \bar{E}) J(\theta, \bar{E}) \\ &= \frac{1}{\varepsilon(E_1, E_2)} \frac{C}{N_\gamma \Omega N_t} J(\theta, \bar{E}), \end{aligned} \quad (3)$$

where the quantities are defined as follows: C is the total detected scattered photon flux in the region of interest, where the region of interest is bounded by the highest-energy photon which can result from the decay of neutral pions and the Compton scattered bremsstrahlung end point; N_t is the number of scattering centers in the target; Ω is the detector solid angle; N_γ is the incident photon flux corresponding to the region of interest; E_1 and E_2 are the energy end points of the region of interest; J is the Jacobian for the transformation from laboratory to

center-of-momentum (c.m.) coordinates; \bar{E} is the bremsstrahlung-weighted average energy over the region of interest; and ϵ is the detector efficiency for this region, as discussed above.

The number density of protons in the target was

$$N_t = (5.37 \pm 0.11) \times 10^{23} \text{ cm}^{-2}.$$

This density was calculated using the target cell geometry and the measured temperature and pressure of the liquid hydrogen. The quoted error reflects the effects of bubbling in the target and fluctuations in the pressure that were observed during the experiment. The detector solid angle Ω was calculated with a Monte Carlo code. The combined effects of the extended target and finite beam size increased the solid angle by 1–2% over the geometrical solid angle. The incident photon flux N_γ was determined from the quantameter by comparing the energy deposited in the quantameter to that which would be deposited by a calculated “known” bremsstrahlung spectrum. An EGS4 simulation of the quantameter verified that its response was, in fact, energy independent and that its calibration constant was reasonable. The detection efficiency ϵ was determined from the EGS4 simulation of the detector. For the energies we measured, the overall detection efficiency was approximately 50%, most of the reduction being due to the beryllium absorber placed in the aperture of the detector.

The kinematic region of interest in the scattered photon spectrum was subdivided into one or more intervals according to the following scheme, made necessary by the combined effects of the Jacobian for the transformation from laboratory to c.m. coordinates and by the significant recoil momentum of the proton. In the calcu-

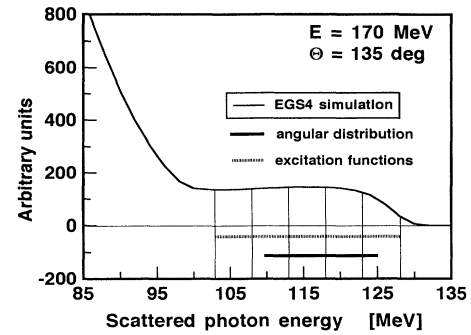


FIG. 4. A smoothed EGS4 simulation illustrating the location of the regions of interest used to extract angular distributions and excitation functions. 5-MeV wide bins are situated within the kinematically allowed region as indicated by the vertical lines in the figure. The heavy horizontal line indicates the approximate region used in the calculation of the angular distribution cross sections.

lation of the angular distributions, a representative average energy was chosen and the end points of the bin were then adjusted (within the kinematic region of interest) to preserve the average energy but to make the bin as large as possible. The results of this procedure are illustrated in Fig. 4 for an end-point energy of 170 MeV and $\theta_{\text{lab}} = 135^\circ$. The solid horizontal line shows the region of the measured spectrum which was used in the calculation of the 141° c.m. point in the 149-MeV angular distribution. The cross sections presented in Table I result from this procedure.

The energy dependence of the differential cross sections at fixed c.m. angles can also be extracted from our

TABLE I. Angular distributions of differential cross sections.

Bremsstrahlung weighted average lab energy (MeV)	c.m. angle	Differential cross section		
		(nb/sr)	Statistical error (nb/sr)	Systematic error (nb/sr)
286	31	217	38	8
	49	183	20	7
	72	160	9	6
	91	163	11	6
	123	188	11	7
	144	228	11	9
230	30	52.0	5.5	1.9
	54	53.2	4.2	2.0
	89	55.6	3.3	2.1
	119	72.3	3.1	2.7
	140	96.0	3.4	3.6
	142	88.4	3.0	3.2
182	31	13.5	2.2	0.5
	60	17.2	1.0	0.6
	90	24.4	1.4	0.9
	114	34.5	1.4	1.3
	141	46.4	1.6	1.7
149	51	6.06	0.60	0.23
	67	7.94	1.38	0.29
	91	13.1	0.5	0.5
	140	27.4	1.0	1.0

data. In order to determine this energy dependence, it was necessary to modify the above method slightly by dividing the region of interest into one or more bins, each approximately 5-MeV wide. This particular width was chosen since it is the smallest interval that exceeds the detector resolution for all of the energies measured in this experiment. These bins were usually positioned so that the high-energy end of the highest-energy bin was about 2

MeV below the end point in the detected (scattered) spectrum. The horizontal dashed line in Fig. 4 shows the approximate region which was used in the calculation of "excitation function" cross sections. The vertical lines delineate the approximate boundaries of the five bins which could be contained in the kinematically allowed region. These "constant bin-width" cross sections are presented in Table II.

TABLE II. Differential cross sections: excitation functions.

c.m. angle (deg)	Bremsstrahlung weighted average lab energy (MeV)	Differential cross sections		
		(nb/sr)	Statistical error (nb/sr)	Systematic error (nb/sr)
31	176	6.0	3.8	0.2
	181	12.9	4.1	0.5
	186	15.7	5.2	0.6
	192	17.1	6.0	0.7
	227	40	9	2
	232	47	10	2
	237	56	15	2
	285	241	50	9
	290	198	74	8
49	284	174	26	7
	290	223	33	9
51	135	7.09	1.58	0.30
	140	6.79	1.24	0.29
	146	6.54	1.16	0.28
	151	4.80	0.97	0.21
	157	6.71	1.26	0.29
	162	7.08	1.83	0.31
	180*	16.2*	2.2*	0.6*
	186*	16.8*	2.3*	0.8*
	192*	18.0*	2.5*	1.1*
	238*	76*	10*	4*
	282*	171*	28*	8*
	291*	223*	34*	10*
	54	226	41.5	7.3
232		43.2	7.1	1.6
237		77.7	9.6	3.0
60	174	15.1	2.1	0.6
	180	17.3	1.7	0.7
	186	17.5	1.8	0.7
	192	19.4	2.4	0.8
	197	12.8	5.3	0.6
67	138	7.4	4.0	0.3
	144	4.2	3.0	0.2
	149	8.1	2.8	0.3
	150	7.5	2.6	0.3
	155	9.8	2.2	0.4
	156	9.3	2.7	0.4
	161	12.4	1.9	0.5
	162	7.2	3.2	0.3
	167	17.4	2.2	0.7
	167	14.1	5.1	0.6
	173	14.2	3.1	0.6
178	12.2	8.4	0.6	
72	283	152	11	6
	290	181	15	7

TABLE II. (Continued).

c.m. angle (deg)	Bremsstrahlung weighted average lab energy (MeV)	Differential cross sections		
		(nb/sr)	Statistical error (nb/sr)	Systematic error (nb/sr)
90	132	12.2	1.2	0.5
	139	12.8	1.1	0.5
	145	11.3	0.9	0.4
	152	13.9	0.8	0.5
	158	16.7	0.9	0.7
	165	22.8	1.6	0.9
	172	21.8	2.7	0.8
	179	22.1	2.6	0.9
	186	24.6	2.6	1.0
	192	31.2	3.1	1.2
	223	48.4	4.7	1.8
	230	52.8	5.0	2.0
	238	81.5	7.3	3.2
	282	152	12	6
113	289	196	17	8
	171	27.0	2.3	1.0
	179	31.7	2.2	1.2
	186	38.5	2.4	1.5
	194	46.6	3.6	1.8
119	222	53.4	3.5	2.0
	231	72.4	4.2	2.8
	239	128	9	5
122	281	172	9	7
	291	239	16	10
141	130	22.0	1.7	0.8
	138	25.3	1.6	1.0
	146	24.1	1.6	0.9
	154	29.8	1.8	1.1
	162	40.8	2.4	1.6
	170	56.0	2.4	2.1
	179	44.2	2.3	1.7
	188	46.4	2.7	1.8
	196	68.6	6.4	2.8
	222	73.0	3.4	2.8
		71.7	3.1	2.7
	232	99.3	4.3	3.8
		96.3	3.9	3.6
282	193	9	8	

E. Systematic errors

The single largest source of systematic error was the 3% error in the calibration of the quantameter. The next largest is the 2% uncertainty in target thickness due to bubbling in the liquid-hydrogen target. The error in the determination of the overall detection efficiency was usually around 0.3% and reflects the statistics of the Monte Carlo detector simulation. The error in the solid angle was also about 0.3% and is also due to the statistical uncertainty of the simulation. The systematic errors quoted in Tables I and II are obtained by summing in quadrature these individual errors. A sum in quadrature is justified since the dominant sources of systematic error are uncorrelated.

IV. RESULTS AND DISCUSSION

We discuss our results within the context of an analysis based on dispersion relations, which link the photon

scattering amplitudes to integrals over the multipole amplitudes for pion photoproduction. There have been many attempts over the years to apply this approach to Compton scattering from the proton. All such attempts are semiphenomenological in that both the experimentally measured photopion amplitudes as well as various theoretical ansatz's are ingredients to the calculation. The approach we will use is based on the work of L'vov [24], which we now describe.

A. Dispersion relation analysis

For photon scattering from a spin- $\frac{1}{2}$ particle, there are six independent invariant amplitudes which one can express in terms of the usual Mandelstam variables s and t . Those amplitudes are written as a sum of Born and dispersive parts. The Born parts, in which the intermediate state is a nucleon, can be calculated exactly given the

charge and magnetic moment of the particle and the usual Feynman rules. For the proton, the Born terms lead to the so-called Powell cross section [1], which dominates for energies well below the pion threshold and satisfies the usual low-energy theorems. The dispersive part is related to the photoabsorption multipole amplitudes via fixed- t dispersion relations. For that part of the total photoabsorption due to single-pion photoproduction, the multipole amplitudes have been extracted from a variety of data and are known reasonably well. This contribution to the dispersion integrals can be calculated reliably, unambiguously, and with an accuracy that is limited only by the accuracy with which the multipole amplitudes have been measured. This is not true for multiple-pion photoproduction, for which some combination of experimental data and theoretical model are needed to determine the multipole amplitudes. In L'vov's treatment, the bulk of the two-pion photoproduction cross section is assumed to occur through a nonresonant π - Δ intermediate state. The multipole amplitudes are then calculated in the Born approximation, assuming single-pion exchange. The s -wave part of that cross section is renormalized in order that the experimental values for the total two-pion photoproduction cross section agree with the calculation. Over the energy range of the present experiment, the one-pion contribution to the dispersion integrals is expected to dominate, so that the predicted cross sections should be only weakly dependent on the theoretical assumptions that go into the calculation of the two-pion part. Photoproduction of greater than two pions is not expected to be important over our energy range and is ignored in this treatment.

In L'vov's treatment, all dispersion integrals are truncated at 1.5 GeV, and the omitted contributions are calculated using a Regge-pole model. In effect, these asymptotic contributions are treated as being equivalent to t -channel exchange diagrams. For four of the six invariant amplitudes (those not involving a photon helicity flip), the asymptotic parts fall off rapidly enough with energy that this Regge procedure does not introduce any strong model dependence to the scattering cross section below 400 MeV. For the remaining two amplitudes (those involving a photon helicity flip), the asymptotic parts do not converge rapidly with energy; as a consequence, they have a non-negligible contribution to the scattering cross section even for energies below 100 MeV. For one of these amplitudes, the asymptotic part is dominated by the t -channel exchange of a neutral pion, giving rise to the so-called Low amplitude [24], which can be reliably calculated since the πNN and $\pi\gamma\gamma$ couplings are well-known experimentally. The remaining amplitude has an asymptotic part due to the exchange of scalar mesons, for which the couplings are only poorly known. In order to resolve this problem, one relies on a low-energy theorem which states that the lowest-order correction to the Powell cross section involves two structure constants, the electric ($\bar{\alpha}$) and magnetic ($\bar{\beta}$) polarizabilities of the proton [3]. The sum of the polarizabilities as given by Eq. (2) is well determined from the forward dispersion relation. One can also write a forward dispersion relation for the difference $\bar{\alpha} - \bar{\beta}$ [24,25], which involves, apart from an in-

tegral over the multipole amplitudes, the $t=0$ limit of the unknown asymptotic part. In L'vov's approach, $\bar{\alpha} - \bar{\beta}$ is treated as the only free parameter, and is used to fix the unknown asymptotic amplitude. One still needs a theoretical ansatz for the t dependence of the amplitude, but for photon energies below 400 MeV, the contribution of that amplitude to the scattering cross section is expected to depend only weakly on t .

To summarize, the Compton scattering cross section in the region from pion threshold to the Δ resonance is predicted using dispersion relations. The cross section is expected to be dominated by those parts of the amplitudes that can be reliably calculated, using as ingredients the Born terms, the one-pion multipole amplitudes, the Low amplitude, and $\bar{\alpha} - \bar{\beta}$. In the calculations to be discussed below, we have used the multipole amplitudes of Arndt [26] and the generally accepted sign [24] for the Low amplitude. We have treated $\bar{\alpha} - \bar{\beta}$ as a free parameter to be determined by a fit to the scattering data. As noted, the cross section is not expected to be very sensitive to less well-known contributions, such as the multipion multipole amplitudes and the other asymptotic amplitudes.

B. Discussion of results

Figures 5(a)–5(d) show the four most complete angular distributions together with the theoretical angular distributions calculated from the dispersion relation analysis (where available, data points from previous experiments are also indicated). Following the standard practice, angles and cross sections are calculated in the c.m. frame while energies are given in the laboratory. The curves in the figures represent the theoretical cross sections for three choices of $\bar{\alpha} - \bar{\beta}$ (0, 5.5×10^{-4} , and $10 \times 10^{-4} \text{ fm}^3$) and provide a visual indication of the sensitivity to this parameter. We note that the theoretical curves converge at forward angles and separate at backward angles. This is consistent with expectations based on the low-energy expansion of the cross section from which one finds that the sensitivity to $\bar{\alpha} - \bar{\beta}$ is greatest at the largest angles. The theory of L'vov is seen to give a good general description of the data in all cases. The present results agree reasonably well with the Illinois data of Bernardini *et al.* [11] and with the Moscow data of Baranov *et al.* [13] but disagree strongly with the Bonn measurements of Genzel *et al.* [15]. The Bonn data [15] portrayed by the triangles in Fig. 6(d) are rather close to the unitarity bound on the Compton scattering cross section, as derived from pion photoproduction amplitudes. This bound represents the lowest conceivable cross section which would obtain in the absence of any real amplitudes, and as such is a model-independent statement. The proximity of earlier data to this bound had been a source of concern for years [8], but as Benmerrouche and Mukhopadhyay [27] have recently pointed out, this problem has been removed by our new measurements.

We have obtained an estimate for the polarizability difference by performing a simultaneous least-squares fit to all of the differential cross sections presented in Table I, using the L'vov formalism. This yields

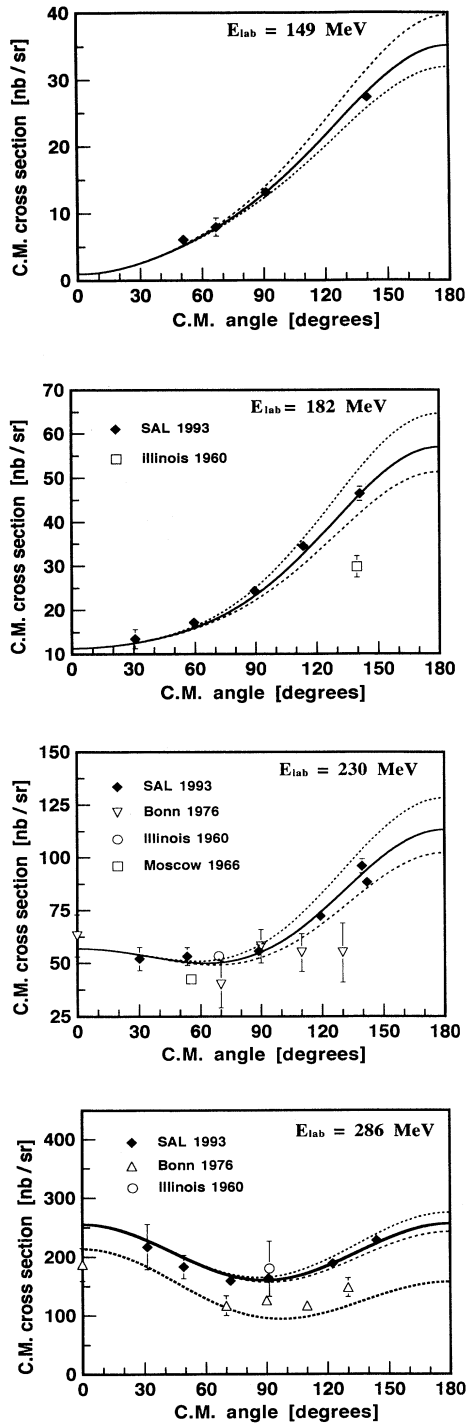


FIG. 5. Angular distributions for 149, 182, 230, and 286 MeV average incident photon energies. Angles are in the c.m. frame and energies are in the laboratory. The curves are calculated from the dispersion theory of L'vov; the upper dashed curves result when $\bar{\alpha} - \bar{\beta} = 0$ and the lower when $\bar{\alpha} - \bar{\beta} = 10$. A simultaneous least-squares fit to all these data, as indicated by the solid curves, yields a value of $(5.5 \pm 0.7 \pm 2.1) \times 10^{-4} \text{ fm}^3$. Data available from previous experiments are also shown. The dash-dotted curve in Fig. 6(d) indicates the unitarity bound for $E_{lab} = 286$ MeV.

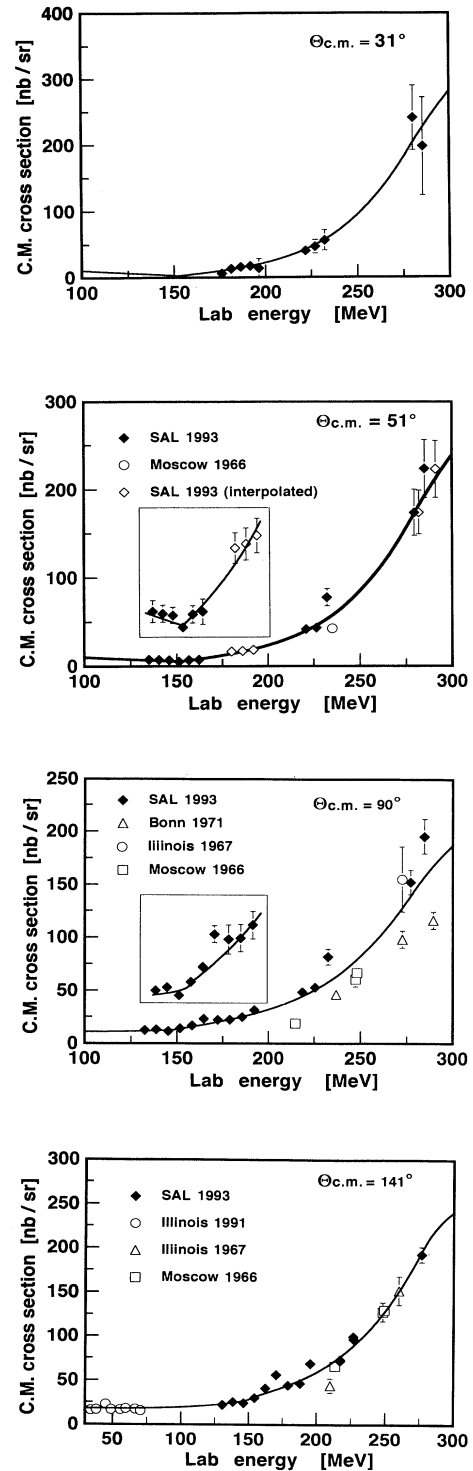


FIG. 6. Excitation curves for c.m. angles 31° , 51° , 90° , and 141° . Energies are in the laboratory frame. These excitation curves serve as a consistency check since the data quoted on a single curve span many runs with different endpoint energies. Data from this and previous experiments (where available) are usually consistent with the one parameter "best-fit" curve, shown by the solid lines. The insets indicate the threshold behavior of the cross sections using an expanded vertical scale.

$$\bar{\alpha} - \bar{\beta} = (5.5 \pm 0.7 \pm 2.1) \times 10^{-4} \text{ fm}^3, \quad (4)$$

where the first error is statistical and the second is systematic. The reduced chi square was $\chi^2_\nu = 0.97$ for 20 degrees of freedom. The following values for the electric and magnetic polarizabilities are inferred using Eq. (2):

$$\begin{aligned} \bar{\alpha} &= (9.8 \pm 0.4 \pm 1.1) \times 10^{-4} \text{ fm}^3, \\ \bar{\beta} &= (4.4 \mp 0.4 \mp 1.1) \times 10^{-4} \text{ fm}^3. \end{aligned} \quad (5)$$

These results compare favorably with a previous measurement by Federspiel *et al.* [4] at Illinois who concluded that $\bar{\alpha} = (10.9 \pm 2.2 \pm 1.3) \times 10^{-4} \text{ fm}^3$ and $\bar{\beta} = (3.3 \pm 2.2 \mp 1.3) \times 10^{-4} \text{ fm}^3$. The Illinois group used NaI crystals and a photon tagging spectrometer in a manner which is conceptually similar to the present work. Our results are also consistent with a more recent measurement by Zieger *et al.* [28] at Mainz who obtained $\bar{\alpha} = (10.6 \pm 1.2 \pm 1.1) \times 10^{-4} \text{ fm}^3$ and $\bar{\beta} = (3.6 \pm 1.2 \pm 1.1) \times 10^{-4} \text{ fm}^3$. The Mainz experiment [28] was performed by momentum analyzing the forward scattered protons from a liquid-hydrogen target; cross sections were then calculated by comparing the forward Compton proton yield with the forward Compton electron yield.

A comparison among the three recent measurements of $\bar{\alpha} - \bar{\beta}$ is given in Table III. Another way to demonstrate the overall consistency of these measurements is to perform a simultaneous least-squares fit to all three sets of cross sections, with each cross section weighted by its statistical error (but not its systematic error). We find a value

$$(\bar{\alpha} - \bar{\beta})_{\text{all}} = (5.8 \pm 0.7) \times 10^{-4} \text{ fm}^3, \quad (6)$$

where the error is therefore only the statistical error. This technique does not permit an evaluation of a systematic error.

C. Model dependency

In each of these experiments, the absolute cross sections are in reasonable agreement with the theoretical calculations of L'vov even before $\bar{\alpha} - \bar{\beta}$ is optimized. This is an important verification of the theory in the lower-energy region where the explicit model dependence is minimal. However, it should be noted that the current analysis is much more sensitive to the details of how Δ is incorporated in the L'vov calculation. A small misfeasance in the treatment of this effect would be much more

TABLE III. Deduced polarizabilities of the proton.

Group	L'vov free parameter $\bar{\alpha} - \bar{\beta}$	Electric polarizability $\bar{\alpha}$ (10^{-4} fm^3)	Magnetic polarizability $\bar{\beta}$
Present work (SAL)	$5.5 \pm 0.7 \pm 2.1$	$9.8 \pm 0.4 \pm 1.1$	$4.4 \mp 0.4 \mp 1.1$
Federspiel <i>et al.</i> [4] (Illinois)	$7.6 \pm 4.3 \pm 2.5$	$10.9 \pm 2.2 \pm 1.3$	$3.3 \mp 2.2 \mp 1.3$
Zieger <i>et al.</i> [24] (Mainz)	$7.0 \pm 2.4 \pm 2.1$	$10.6 \pm 1.2 \pm 1.1$	$3.6 \pm 1.2 \pm 1.1$

significant here than for either of the two previous works. In order to investigate the potential significance of such an error, a least-squares fit was performed to several subsets of the data, including the most recent data from Illinois and Mainz [4,28]. First, the fitting procedure included only those data up to 149 MeV. Higher-energy angular distributions were subsequently included in the fit one at a time. The results of this procedure are summarized in Table IV, where no systematic energy dependence of $\bar{\alpha} - \bar{\beta}$ is discernible within the statistical errors.

One possible source of model dependence in the extraction of $\bar{\alpha} - \bar{\beta}$ is the ansatz for the t dependence of the asymptotic contribution to the "A1" Compton amplitude [27], as discussed in Sec. IV A. L'vov's code permits this asymptotic contribution to be constant, to have an exponential t dependence, or to be ignored completely. Depending on the option chosen, the extracted value of $\bar{\alpha} - \bar{\beta}$ varies by about $\pm 1.3 \times 10^{-4} \text{ fm}^3$; at an extremum. Values of $\bar{\alpha} - \bar{\beta}$ quoted in this paper were extracted using the more complicated exponential t dependence as recommended by L'vov [22].

We have also investigated the possibility that the extracted value of $\bar{\alpha} - \bar{\beta}$ may be unduly influenced by the choice of photoproduction amplitudes used as inputs to L'vov's code [29]. There are two compilations which we have used; one due to Arndt *et al.* [24] and one by Metcalf and Walker [30]. The extracted value of $\bar{\alpha} - \bar{\beta}$ is only slightly affected by this choice with the difference between the two approaches being only $0.3 \times 10^{-4} \text{ fm}^3$. All values of $\bar{\alpha} - \bar{\beta}$ quoted in this paper were extracted using the newer compilation of Arndt *et al.*

Finally, we briefly comment on the energy dependence of the experimental cross section. Our complete excitation functions obtain at $\theta_{\text{c.m.}} = 31^\circ, 51^\circ, 90^\circ$, and 141° , and these are displayed in Figs. 6(a)–6(d). The excitation curves serve to check the internal consistency of the measurement and analysis procedure, since the data they represent cover many runs at different end-point energies. The Moscow data of Baranov *et al.* [13] are in generally good agreement with the present results except at 90° . Likewise, the Bonn data are low at 90° . The Illinois data of Gray and Hanson [14] and of Federspiel *et al.* [4] are also well represented by the curve derived from the one-parameter least-squares fit to our angular distributions. It is possible to interpolate, using cubic spline interpolation, some of our angular distribution in order to fill in the gaps in our excitation functions. Where this can be done in a sufficiently accurate and reliable way, the interpolated cross sections have been calculated and are marked with an asterisk in Table II. Interpolated results are presented only when a reasonably complete and

TABLE IV. Energy dependence of $\bar{\alpha} - \bar{\beta}$.

Data range (MeV)	$\bar{\alpha} - \bar{\beta}$ (10^{-4} fm^3)
34–149	5.5 ± 1.5
34–182	4.6 ± 1.0
34–230	5.5 ± 0.7
34–286	5.8 ± 0.7

“smooth” angular distribution exists for the energy in question. These interpolated cross sections are a product of the analysis and were never used as input “data” in our determination of $\bar{\alpha}$ and $\bar{\beta}$.

In summary, our measurements provide systematic and complete angular distributions for Compton scattering from the proton, in an energy and angular range for which data were not previously available. Previous measurements are in reasonable agreement with the current results, with the notable exception of the Bonn data [15]. In all regions the data are consistent with dispersion relation predictions as constrained by dispersion sum rules. This good agreement with the model and with previous experiments allows a comparatively reliable extraction of the electric and magnetic polarizabilities of the proton. The deduced values are sufficiently precise to suggest that

the difference $\bar{\alpha} - \bar{\beta}$ is smaller than but still consistent with, previously measured values. The deduced value for $\bar{\beta}$ is higher than those which have been quoted in the past. In addition, we present data which spans the threshold for pion photoproduction; the quality of this data is sufficient to provide some evidence for the so-called “unitarity cusp” in the Compton electric dipole amplitude f_{EE}^{1-} [31].

ACKNOWLEDGMENTS

We gratefully acknowledge A. I. L’vov for providing the computer code used in this analysis. This work was supported in part by the Natural Sciences and Engineering Research Council of Canada and by the National Science Foundation of the United States.

-
- [1] J. L. Powell, *Phys. Rev.* **75**, 32 (1949).
 - [2] D. Drechsel and A. Russo, *Phys. Lett.* **137B**, 294 (1984).
 - [3] A. I. L’vov, Proceedings of the Workshop on Hadron Structure from Photo-reactions at Intermediate Energies, Brookhaven National Laboratory, 1992 (Report No. BNL 47972), p. 33; V. A. Petrun’kin, *Fiz. Elem. Chastits At. Yadra* **12**, 692 (1981) [*Sov. J. Part. Nucl.* **12**, 278 (1981)].
 - [4] F. J. Federspiel *et al.*, *Phys. Rev. Lett.* **67**, 1511 (1991).
 - [5] A. C. Hearn and E. Leader, *Phys. Rev.* **126**, 789 (1962).
 - [6] R. Koberle, *Phys. Rev.* **166**, 1558 (1968).
 - [7] I. Guiascu, C. Pomponiu, and E. E. Radescu, *Ann. Phys.* **114**, 296 (1978).
 - [8] W. Pfeil, H. Rollnik, and S. Stakowski, *Nucl. Phys.* **B73**, 166 (1974).
 - [9] M. Gell-Mann, M. L. Goldberger, and W. E. Thirring, *Phys. Rev.* **95**, 1612 (1954); M. Damashek and F. J. Gilman, *Phys. Rev. D* **1**, 1319 (1970).
 - [10] E. C. Booth and J. P. Miller, SAL Report 007, 1986 (unpublished).
 - [11] Bernardini *et al.*, *Nuovo Cimento* **18**, 1203 (1960).
 - [12] J. W. DeWire *et al.*, *Phys. Rev.* **124**, 909 (1961).
 - [13] P. S. Baranov *et al.*, *Yad. Fiz.* **3**, 1083 (1960) [*Sov. J. Nucl. Phys.* **3**, 791 (1966)].
 - [14] E. R. Gray and A. O. Hanson, *Phys. Rev.* **160**, 160 (1967).
 - [15] H. Genzel *et al.*, *Z. Phys.* **279**, 399 (1976).
 - [16] J. P. Miller *et al.*, *Nucl. Instrum. Methods A* **270**, 431 (1988).
 - [17] D. Delli Carpini, Ph.D. thesis, Boston University, 1990 (unpublished).
 - [18] W. R. Nelson, H. Hirayama, and D. W. O. Rogers, EGS4 Code System, SLAC-265, 1985.
 - [19] J. L. Matthews and R. O. Owens, *Nucl. Instrum. Methods* **111**, 157 (1973).
 - [20] G. Cocconi and A. Silverman, *Phys. Rev.* **88**, 1230 (1952).
 - [21] H. Genzel, P. Joos, and W. Pfeil, in *Photoproduction of Elementary Particles*, edited by H. Schopper (Springer-Verlag, New York, 1973).
 - [22] D. Delli Carpini *et al.*, *Phys. Rev. C* **43**, 1525 (1991).
 - [23] R. Igarashi, Ph.D. thesis, University of Saskatchewan, 1993.
 - [24] A. I. L’vov, *Yad. Fiz.* **34**, 1075 (1981) [*Sov. J. Nucl. Phys.* **34**, 597 (1981)].
 - [25] A. I. L’vov, V. A. Petrun’kin, and S. A. Startsev, *Yad. Fiz.* **29**, 1265 (1979) [*Sov. J. Nucl. Phys.* **29**, 651 (1979)].
 - [26] R. A. Arndt *et al.*, *Phys. Rev. C* **42**, 1853 (1990).
 - [27] M. Benmerrouche and N. C. Mukhopadhyay, *Phys. Rev. D* **46**, 101 (1992).
 - [28] A. Zieger *et al.*, *Phys. Lett.* **34B**, 38 (1992).
 - [29] A. I. L’vov (private communication).
 - [30] W. J. Metcalf and R. L. Walker, *Nucl. Phys.* **B76**, 253 (1974).
 - [31] J. C. Bergstrom and E. L. Hallin, *Phys. Rev. C* **48**, 1508 (1993), the following paper.